1 Controlling the thickness dependence of torsional wave mode in 2 pipe-like structures with the gradient-index phononic crystal lens 3 4 5 Gorkem Okudan^a, Chenxi Xu^a, Hrishikesh Danawe^b, Serife Tol^b, Didem Ozevin^{a*}, 6 7 ^a Department of Civil, Materials, and Environmental Engineering, University of Illinois at Chicago 8 ^b Department of Mechanical Engineering, University of Michigan 9 * Corresponding author, dozevin@uic.edu, 842 W Taylor Street ERF 2095 Chicago IL 60607 10 11 **Abstract** 12 The fundamental torsional wave mode, T(0,1), is typically preferred in monitoring defects in 13 long-range pipe-like structures due to non-dispersive and low attenuation characteristics such 14 that the wave packet is not distorted with distance. However, the sensitivity of T(0,1) wave mode 15 depends on the defect type and orientation. While it is highly sensitive to cracks along the axis of 16 pipes, the sensitivity to detect thickness change is low as T(0,1) wave mode generates tangential 17 displacement motion around the pipe circumference. In this study, a gradient-index phononic 18 crystal (GRIN-PC) lens is integrated into a steel pipe to manipulate its dispersion characteristics 19 such that the phase velocity of T(0,1) wave mode is affected by the overall change in pipe 20 thickness. The modified behavior of T(0,1) wave mode within the GRIN-PC lens region 21 increases the damage detection capability of T(0,1) wave mode. Numerical models involving a 22 parametric unit cell study indicate that the phase velocity of T(0,1) wave mode decreases as the 23 thickness of the pipe with the GRIN-PC lens decreases, in contrast with the conventional pipe. 24 The signal difference coefficient (SDC) is applied to the acquired signal from the focal point of 25 GRIN-PC lens to quantify the uniform thickness change. Full-scale wave propagation 26 simulations involving solid mechanics coupled with the piezoelectric actuation demonstrate that 27 the SDC increases as the thickness decreases. The numerical results are validated with 28 experiments using three steel pipes with different wall thicknesses. 29 Keywords: torsion mode, pipes, thickness-dependence, phononic crystals, gradient-index lens 30

31

1. Introduction

32

33 Corrosion is one of the leading causes of failure in oil, hazardous liquid, and gas pipelines [1]. 34 Internal corrosion is common in oil pipelines, whereas it does not occur in pipelines that carry 35 dry gas unless they are contaminated with corrosive fluids [2]. Uniform corrosion is the 36 predominant type of internal corrosion [3]. Failure is linked to the decreased strength due to 37 metal loss, resulting in property damage, and even casualties [4]. Techniques such as cathodic 38 protection are meant for the external surface of pipelines, and are not effective against internal 39 corrosion [5]. Early detection of metal loss due to corrosion in steel pipes has been studied in the 40 literature using nondestructive evaluation (NDE) methods [6-11]. Guided wave ultrasonics is a 41 well-known NDE method for corrosion detection in oil and gas pipelines. Honarvar et al. studied 42 the pipe wall erosion/corrosion thinning rates using cross-correlation and model-based estimation 43 applied to ultrasonic data and estimated the thinning rates with good accuracy [12]. They showed 44 that cross-correlation was a numerically more stable and less complex method, compared to a 45 model-based method with a high computational cost. Nagy et al. investigated the corrosion and 46 erosion in steel pipes and other thin-walled structures with a novel approach based on the 47 fundamental flexural wave mode [13]. They took advantage of the difference in the 48 dispersiveness of group and phase velocities at high frequencies, and carried out wall thickness 49 assessment from phase angle measurements within the constant group velocity range of the 50 fundamental asymmetric mode. Corrosion imaging based on guided wave tomography and 51 helically-propagating Lamb wave modes were performed to detect wall thickness changes in 52 metallic pipes [14-16]. Signal difference coefficient (SDC) is a reference-based damage index 53 that has been adopted in order to quantify the statistical difference between two signals, based on 54 the Pearson correlation coefficient [17]. Zhao et al. implemented SDC to examine the growth of 55 corrosion defects in an aircraft wing structure [18]. They associated increasing SDCs with larger 56 corrosion areas relative to the pristine condition. Furthermore, other researchers showed SDC to 57 be a reliable statistical quantity to generate an image of the micro-corrosive defects through 58 guided wave tomography in both plate-like [19, 20] and pipe-like structures [14]. Still, the SDC 59 applied to the T(0,1) wave mode by itself is not sensitive to overall thickness change in a steel 60 pipe, unless the dispersion characteristics are modified. Being insensitive to the change in wall 61 thickness of conventional pipe structures limits the use of torsional wave mode to detect uniform 62 corrosion.

63 Phononic crystals (PCs) are artificially engineered structures that can be designed by periodically 64 adding or embedding inclusions into a base structure [21]. The periodic variation in the geometry 65 or the mechanical properties of the engineered structure results in the deviation of dispersion 66 branches from the base structure. PCs are applied to plate-like and pipe-like structures to 67 manipulate the propagating elastic waves by blocking, redirecting and focusing. Theoretical and 68 numerical studies on vibration reduction in pipes using PCs can be found in the literature [22, 69 23]. A special case of PCs, gradient-index phononic crystals (GRIN-PC), are refractive devices based on Snell's law in optics [24] in which the variation of elastic properties follows a 70 71 hyperbolic secant profile that bends the plane wave towards a focal point [25]. Consequently, 72 propagating elastic waves redirected to a focal point exhibit an increased wave amplitude. In our 73 previous studies, we demonstrated the focusing of guided wave modes in pipe-like structures 74 using a conformal GRIN-PC lens [26, 27]. The amplitudes of the received signals were 75 approximately doubled, which broke the limitation of propagation distance of elastic waves due 76 to attenuation. The influence of GRIN-PC lens to detect uniform corrosion using torsional wave 77 mode and single receiving sensor in hollow structures was not investigated numerically and 78 experimentally. 79 In this paper, we present the control of torsional wave mode to pipe wall thickness change with 80 the GRIN-PC lens. In a pipe-like structure integrated with a GRIN-PC lens, pipe wall thickness 81 change results in a shift in the phase velocity, which modifies the arrival time of torsional wave 82 mode, allowing for the SDC to be used in tracking the thickness loss. We studied the influence of 83 base structure thickness on band diagrams or dispersion curves with the unit cell approach. Six 84 pipes with identical outer diameters but different thicknesses were numerically modeled with and 85 without the GRIN-PC lens using COMSOL Multiphysics software. The models included 86 transmitters and receivers made of piezoelectric transducers as well as the adhesive layer 87 between the sensor-structure interface. The numerical unit cell and the full-scale pipe models are 88 presented in section 2. Three pipes with different thicknesses were experimentally tested 89 simulating the conditions of numerical models. Section 3 includes the description of experiments 90 and the results. The peak frequency was extracted as a feature and the SDC from the time 91 domain was selected as a damage index to quantify the overall thickness change representing the 92 uniform corrosion. The numerical and experimental results show that the detectability of

- thickness change using torsional wave mode and single receiving sensor is achievable with the
- 94 GRIN-PC lens. The conclusions of this study are presented in section 4.

95 **2.** Materials and methods

- In this section, numerical models involving the unit cell and the full-scale pipe structures as well
- as the experimental configuration are described.
- 98 2.1. Specifications of the pipe configuration with the GRIN-PC lens
- 99 The GRIN-PC lens consists of cylindrical stubs that are periodically arranged on the exterior
- surface of a hollow cylindrical structure. The variables of the GRIN-PC lens are stub spacing,
- size and material. The spacing defines the unit cell size, which is selected as 20 mm in this study
- based on the wavelength of the target guided wave mode. The stub size and material affect the
- 103 composite action of the unit cell with respect to base material. In this study, the stub material and
- diameter were selected as structural steel and 10 mm, respectively. The stub height was increased
- from 1 mm to 5 mm based on the refractive index profile as shown in Fig. 1(a). The refractive
- index n of each unit cell is calculated by

$$n = \frac{v}{v_{\Gamma X}} \tag{1}$$

- where ν is the reference phase velocity determined from the plain pipe; $\nu_{\Gamma X}$ is the phase velocity
- 108 of each unit cell for a specific stub height along the ΓX direction of wave vector. The refractive
- index values of different stub heights are fit to the hyperbolic secant profile as:

$$n(s) = n_0 \operatorname{sech}(\alpha s) \tag{2}$$

- where n_0 is the refractive index of the unit cell located at the centerline of the lens, α is the
- gradient coefficient, and s is the circumferential position of the stubs in terms of unit cell size a.
- The focal point of the GRIN-PC lens is determined as $\pi/2\alpha$. The selected stub heights are shown
- in Fig. 1(b). The total array of GRIN-PC lens includes 10 x 13 stubs positioned along axial and
- circumferential directions. The heights of the stubs are 4.50 mm, 4.46 mm, 4.31 mm, 4.06 mm,
- 3.65 mm, 2.96 mm, and 1.92 mm to focus the torsional wave mode at a focal point of 10a [26].

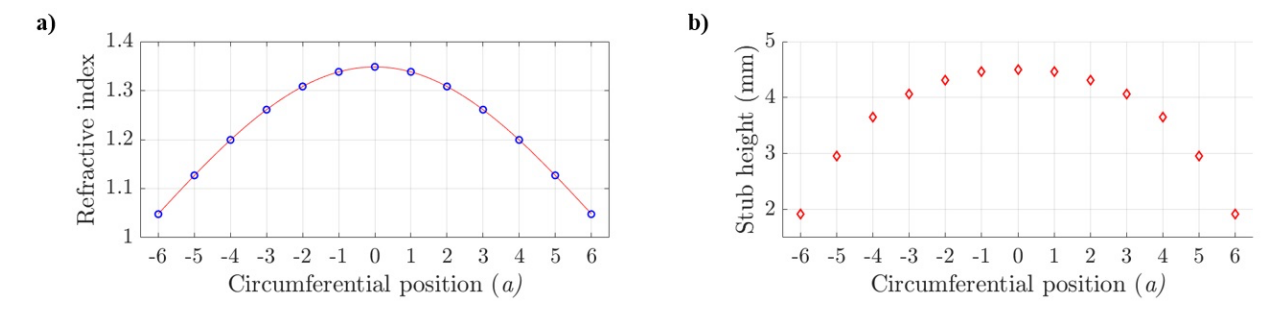


Fig 1. (a) Hyperbolic secant profile fit to the refractive index values of stubs positioned along the pipe circumference normalized to the unit cell size a, and **(b)** corresponding stub heights.

The finalized geometry of GRIN-PC lens is shown in Fig. 2(a). The cross-section of the steel pipe with the GRIN-PC lens, where the stub heights are symmetrically decreasing from the center to the two edges of the lens, is illustrated in Fig. 2(b). The top view of the pipe configuration with the GRIN-PC lens focusing the T(0,1) plane wave can be seen in Fig. 2(c).

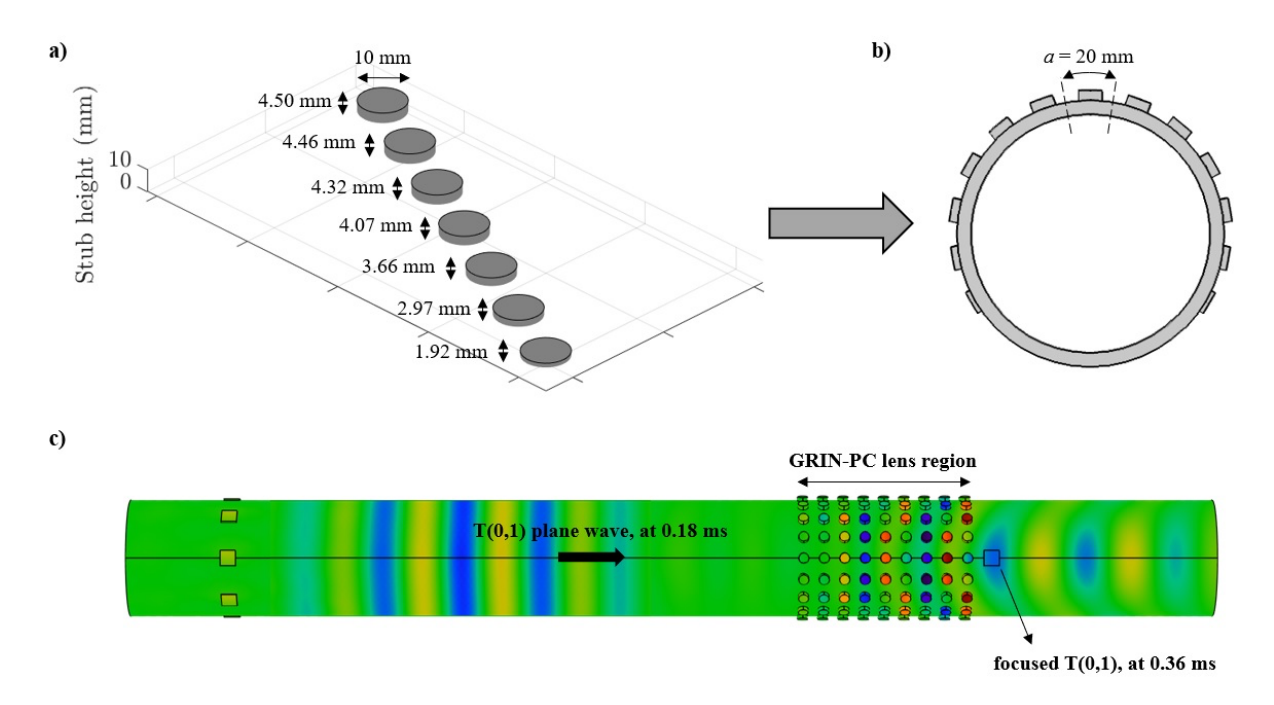


Fig. 2. (a) Steel stubs with varying heights that follow the hyperbolic secant profile. **(b)** The cross-section of the pipe that illustrates the 13-unit cells-wide GRIN-PC lens made of steel stubs. **(c)** The top view of the full-scale steel pipe integrated with the GRIN-PC lens, manifesting the focusing behavior.

2.2.Description of the finite element models

The pipe wall thickness was varied from 6.00 mm to 3.18 mm to simulate the uniform corrosion. Each unit cell model was made of 20 mm x 20 mm slice of the pipe wall, where the pipe wall thickness was gradually decreased as shown in Fig. 3(a). The band diagrams and the dispersion curves were obtained by analyzing the eigenfrequencies of the unit cell in COMSOL Multiphysics. The Bloch-Floquet periodic boundary condition, applicable for pipe-like structures [28], was assigned to the axial and circumferential directions of the unit cell. The wave number was swept along the edge of the first irreducible Brillouin zone. First, the unit cell without any stubs representing conventional pipe was investigated. Then, the unit cell with the 4.5-mm stub, as illustrated in Fig. 3(a), was modeled. The unit cell with the 4.5-mm stub also included a 0.15 mm-thick epoxy adhesive that attached the stub to the pipe surface due to the impact on the dispersion properties as discussed in [27]. The unit cell model with linear tetrahedral mesh is indicated and its boundary conditions are highlighted in Fig. 3(b).

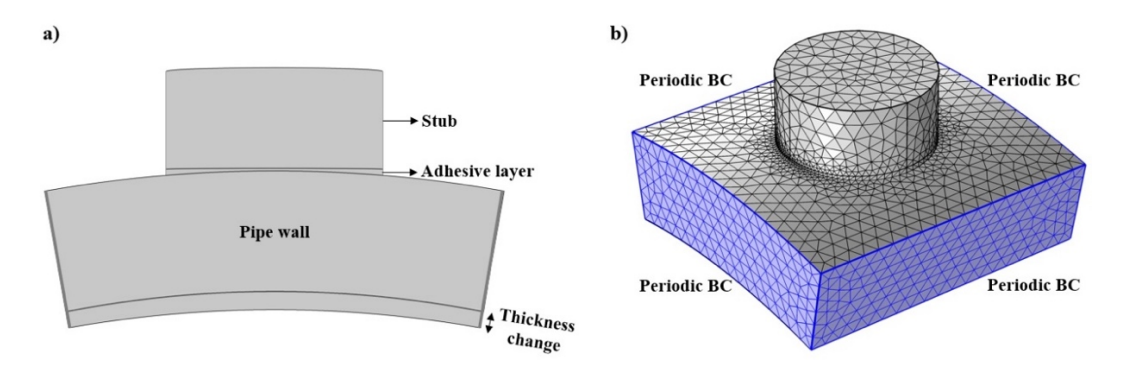


Fig. 3. (a) Front view of the three-dimensional unit cell model with the 4.5 mm stub. Uniform corrosion is simulated as the thickness change of pipe wall. **(b)** Perspective view of the meshed unit cell model indicating the boundary conditions.

Multiphysics numerical models of the full-scale pipe were built with the physical fields of solid mechanics and piezoelectric actuation/detection. The maximum element size of the mesh made of the first-order tetrahedral elements was selected as one-twelfth of the wavelength of the T(0,1) mode. The minimum element size of the mesh was selected as the one-fifth of the maximum size to refine in the GRIN-PC lens region and avoid any abrupt reductions in the element size. Thus, the maximum element size was about 6.6 mm. The time step was determined by conservatively assuming a Courant–Friedrichs–Lewy number of 0.2. Hence, the time step was selected as 0.33

μs. The total mesh of the plain pipe consisted of 79,603 domain elements, 44,020 boundary elements, and 1,365 edge elements. The total mesh of the pipe with the GRIN-PC lens consisted of 150,857 domain elements, 75,792 boundary elements, and 6,236 edge elements. The selected frequency of guided wave in the pipe model was 40 kHz, within the preferred range of frequencies to detect defects in pipelines [29]. A seven-cycle Hanning window loading function with a center frequency of 40 kHz was applied to an array of eight d35 mode piezoelectric actuators with the dimensions of 15 mm x 15 mm x 1 mm to generate the plane torsional wave mode. In this study, the through-transmission configuration of guided wave ultrasonic testing was preferred, which is illustrated in Fig. 4(a). The full-scale pipe configuration with an array of actuators to excite the T(0,1) mode and a receiver at 10*a*, is shown in Fig. 4(b). The arrangement of the GRIN-PC lens on the same pipe model is shown in Fig. 4(c). The overall mesh schemes of the plain pipe and the pipe with the GRIN-PC lens are shown in Fig. 4(d) and 4(e), respectively.

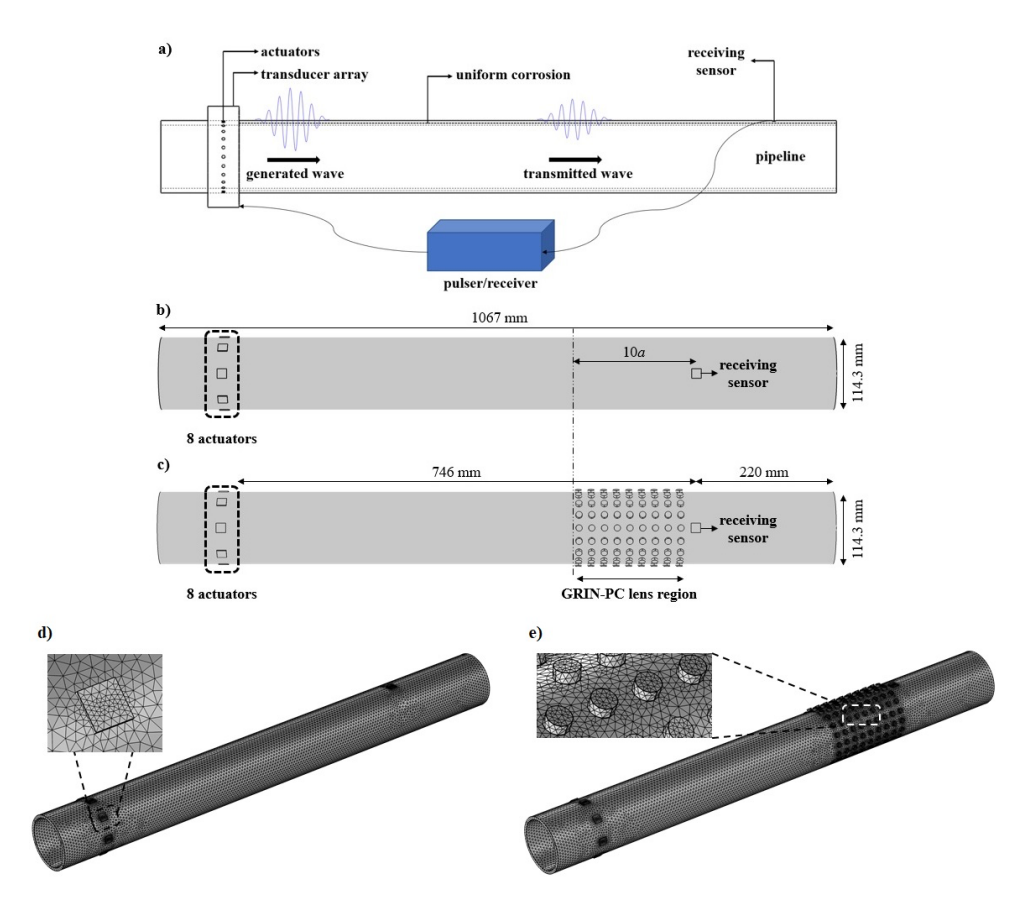


Fig. 4. (a) Through-transmission configuration of guided wave ultrasonic testing. **(b)** Full-scale finite element model of the plain pipe and **(c)** the pipe with the GRIN-PC lens. **(d)** The overall mesh scheme of the plain pipe and **(e)** the pipe with the GRIN-PC lens.

The constant dimensional variables were 114.3 mm as the outer diameter, 1067 mm as the total length, and 746 mm as the distance between the transducer array and the receiving sensor.

Traction-free boundary conditions were defined at the edges of the pipe to simulate the experimental condition. The density, Young's Modulus, and Poisson's ratio of the structural steel were defined as 7850 kg/m³, 200 GPa, and 0.30, respectively. The density, Young's Modulus, and Poisson's ratio of the epoxy were defined as 1700 kg/m³, 2.7 GPa, and 0.45, respectively.

The properties of the piezoelectric material in the models are summarized in Table 1.

Table 1. Properties of the piezoelectric material.

| d ₃₅ (10 ⁻¹² C/N) | 590 |
|---|------|
| E33 | 3400 |
| Y ^E ₁₁ (GPa) | 63 |
| Y ^E ₃₃ (GPa) | 54 |

In Table 1, d_{35} is piezoelectric coupling coefficient, ϵ_{33} is electric permittivity constant, Y^E_{11} is Young's Modulus in the longitudinal direction, and Y^E_{33} is Young's Modulus in the transverse direction. Electrodes were placed on the top and bottom surfaces of piezoelectric element, resulting in an electric field applied along the vertical direction. To model each transducer at different position around the pipe circumference, the local coordinates of each transducer were rotated in COMSOL Multiphysics software.

2.3.Description of the experiments

Three steel pipes with different wall thicknesses (i.e., 6.00 mm, 4.75 mm, 3.18 mm) with the same outer diameter of 114.3 mm were investigated to simulate the uniform thickness loss due to corrosion. The images of the three pipes are shown in Fig. 5. The lengths of the 4.75 mm and 3.18 mm pipes were the same as their numerical counterparts, 1067 mm, while the length of the 6.00 mm pipe was 1500 mm. The pipe with 6 mm thickness also had the ends enclosed as this pipe was used to simulate leak in our prior work [30].



192

193

202

Fig. 5. Experimental configuration showing steel pipes with wall thickness of (a) 6 mm, (b) 4.75 mm, (c) and 3.18 mm.

- An array of eight d35 mode APC 850 piezoelectric plates from American Piezo with dimensions
- of 15 mm x 15 mm x 1 mm, were uniformly arranged around the circumference of each pipe.
- 196 The array was placed 100 mm away from the edge, and coupled to the pipe surface using epoxy.
- Another APC 850 piezoelectric plate was mounted at 10a position as the receiver. The excitation
- signal was a seven-cycle sine burst signal with the peak frequency at 40 kHz and the bandwidth
- of 35.8-44.2 kHz (defined as \pm 3 dB change). The receiving sensor was connected to a pre-
- amplifier with 40 dB gain. The data was collected using a PCI-8 data acquisition system
- 201 manufactured by MISTRAS with a sampling rate of 1 MHz and a digital filter of 20-200 kHz.

3. Results and discussion

- 203 3.1.Numerical results
- 204 3.1.1. Parametric unit cell study of thickness change
- 205 Band diagrams corresponding to each wave mode were obtained by extracting the frequency and
- 206 wave number data from the periodic unit cell simulations. Dispersion curves of the wave modes
- were generated by converting the frequency and wave number to phase velocity based on the
- 208 relationship:

$$c_p = \frac{2\pi f}{k} \tag{3}$$

where c_p is the phase velocity, f is the frequency, and k is the wave number. Since the unit cell approach was used to compute the dispersion curves, the bands were bounded by the limits of the Brillouin zone at $-\pi/a$ and π/a . Thus, the wave vector was corrected after the boundary at π/a by folding the next band in the first Brillouin zone. The band diagram for a steel pipe with 6 mm wall thickness indicating the snapshots of the propagating mode shapes for the L(0,1), L(0,2), and T(0,1) wave modes is shown in Fig. 6.

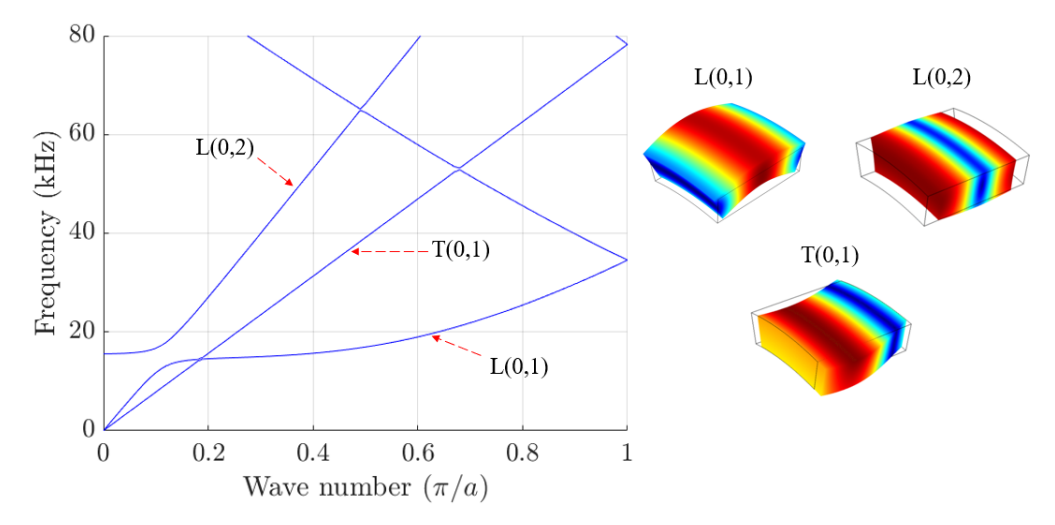


Fig. 6. Band diagram for the pipe with 6 mm wall thickness depicting the axisymmetric wave modes (L(0,1), L(0,2), and T(0,1)) and their mode shapes.

In this case, the phase velocity was calculated using the equation:

$$c_p = \frac{2\pi f}{\frac{2\pi}{a} - k} \tag{4}$$

where a is the unit cell size. The band diagrams are shown in Fig. 7(a) and 7(b) for the plain pipe and the stubbed cases, respectively. Similarly, the dispersion curves are illustrated in Fig. 7(c) and 7(d) for the plain pipe and the stubbed cases, respectively.

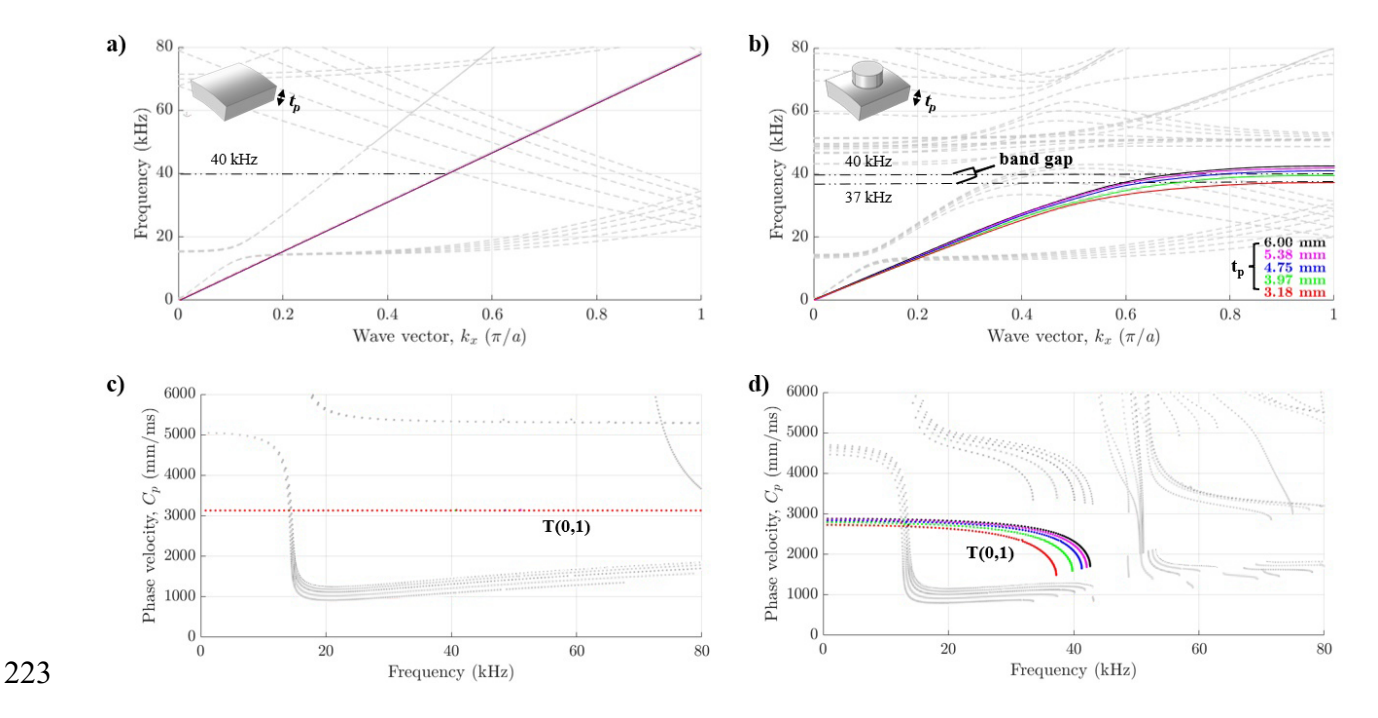


Fig. 7. Band diagrams of the steel pipe with varying wall thicknesses, **(a)** without any stubs, and **(b)** with the 4.5-mm stub along with the 0.15-mm epoxy layer. Dispersion curves of the steel pipe with varying wall thicknesses, **(c)** without any stubs, and **(d)** with the 4.5-mm stub along with the 0.15-mm epoxy layer.

In the band diagrams, the colored lines represent the bands only for the T(0,1) mode at different thicknesses. As it can be observed from the plain unit cell in Fig. 7(a), the bands for the T(0,1) mode are straight lines emerging from the origin and aligned with each other, whereas for the unit cell with a stub height of 4.5 mm, the band diagram changes depending on the base thickness, as seen in Fig. 7(b). The change in the phase velocity can be determined from the dispersion curves in Fig. 7(c) and 7(d). In this case, the T(0,1) wave mode is shown in a color scheme in which different colors correspond to varying thicknesses. For the plain unit cell, the phase velocity of the T(0,1) mode remains unchanged at any studied thickness. Thickness of a guided structure influences the phase velocity due to the reflections and mode conversions of propagating wave between inner and outer surfaces. In the case of T(0,1) wave mode, the particle motion is parallel to surface; therefore, its phase velocity does not depend on thickness. For the unit cell with the stub height of 4.5 mm, a band gap forms and becomes wider as the wall thickness decreases. The T(0,1) band of the 3.18 mm-thick pipe wall with the stub has a maximum value of 37 kHz, implying that the T(0,1) mode cannot propagate above that level.

However, as the GRIN-PC lens consists of stubs with various heights that are smaller than 4.5 mm, the band gap does not affect overall wave propagation, which was verified with full-scale simulations in Section 3.1.2. Finally, the results from the unit cell simulations suggest that, as the pipe wall thickness gradually decreases from 6.00 mm to 3.18 mm, the phase velocity of the T(0,1) mode does not change in the conventional pipe structure; nevertheless, with the presence of the 4.5-mm stub in the unit cell, the phase velocity of T(0,1) decreases.

3.1.2. Full-scale multiphysics simulations

The waveforms obtained from the receiving sensor at 10a for the pipes with 6 mm, 4.75 mm, and 3.18 mm wall thicknesses are plotted for the plain pipe and the GRIN-PC lens cases in Fig. 8(a) and 8(b), respectively. The waveforms in the frequency domain were obtained by applying the Fast-Fourier Transform (FFT) to the T(0,1) window demonstrated for the plain pipe and the GRIN-PC lens cases in Fig. 8(c) and 8(d), respectively. The frequency spectra of time history signals were normalized to their peak values to emphasize the shifts in the peak frequency with the pipe thickness.

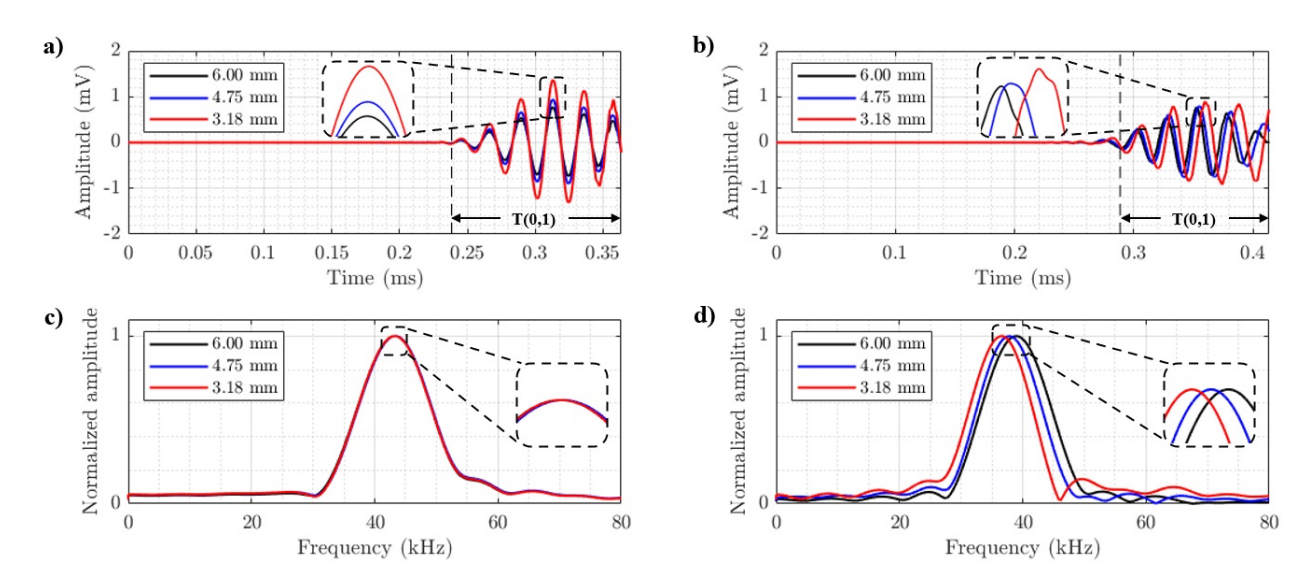


Fig. 8. Numerical waveforms in the time domain for the 6.00 mm, 4.75 mm, and 3.18 mm wall thicknesses, obtained from 10*a* location in the case of (a) the plain pipe, (b) and the pipe with the GRIN-PC lens. Normalized frequency spectra of time history signals for the 6.00 mm, 4.75 mm, and 3.18 mm pipe thicknesses, obtained from 10*a* location in the case of (c) the plain pipe, (d) and the pipe with the GRIN-PC lens.

262 The wave packet corresponding to the T(0,1) mode is identified in Fig. 8(a) and 8(b), based on 263 the theoretical arrival time of T(0,1) mode. For the plain pipe, the T(0,1) mode for all pipe 264 thicknesses remains in the same phase. For the pipe with the GRIN-PC lens, the shift in the T(0,1) mode is clearly visible, and it is due to the changes in dispersion characteristics with the 265 266 presence of the GRIN-PC lens. The frequency domain of the T(0,1) window implies that the 267 peak frequency barely changes from 43.22 kHz at 6 mm thickness, to 43.24 kHz at 4.75 mm, and 268 to 43.35 kHz at 3.18 mm wall thickness, in the case of the plain pipe, as observed in Fig. 8(c). 269 However, for the pipe with the GRIN-PC lens, the peak frequency decreases from 38.94 kHz to 270 37.84 kHz, and then to 36.56 kHz, as the overall pipe thickness decreases from 6 mm to 4.75 271 mm, and then to 3.18 mm, as seen in Fig. 8(d). In summary, the GRIN-PC lens modifies the 272 phase velocity of the T(0,1) mode depending on the base thickness, which leads to shifts in the 273 arrival times of the T(0,1) mode. Furthermore, as the thickness decreases, the peak frequency 274 shifts further away from 40 kHz for this GRIN-PC lens configuration because the dominant 275 torsional frequency is reduced with thickness reduction as seen in Fig. 8(d). Hence, the GRIN-276 PC lens allows for more sensitivity to thickness change with the ultrasonic T(0,1) wave mode as 277 compared to the conventional steel pipe. 278 3.2.Experimental validation 279 A procedure similar to the numerical demonstration was followed to analyze the experimental 280 results. The waveforms obtained from the focal point for the pipes with 6 mm, 4.75 mm, and 281 3.18 mm wall thicknesses are plotted for the plain pipe and the GRIN-PC lens cases in Fig. 9(a)

and 9(b), respectively. The waveforms in the frequency domain were obtained by applying the

FFT to each T(0,1) window, and they are demonstrated for the plain pipe and the GRIN-PC lens

282

283

284

cases in Fig. 9(c) and 9(d), respectively.

13

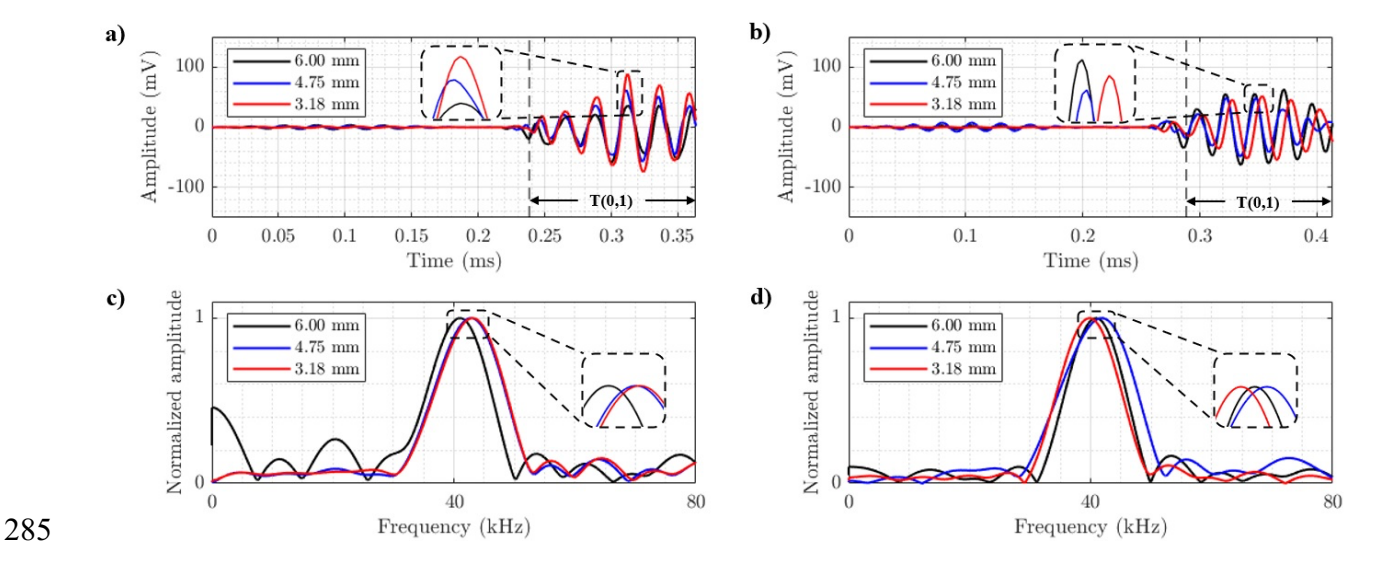


Fig. 9. (a) Experimental waveforms in the time domain for the 6.00 mm, 4.75 mm, and 3.18 mm wall thicknesses, obtained from 10*a* location in the case of the plain pipe, **(b)** and the pipe with the GRIN-PC lens. **(c)** Normalized frequency spectra of time history signals for the 6.00 mm, 4.75 mm, and 3.18 mm pipe thicknesses, obtained from 10*a* location in the case of the plain pipe, **(d)** and the pipe with the GRIN-PC lens.

287

288

289

290

291

292

293

294

295

296

297

298

299

300

301

302

303

304

305

306

In the time domain, the T(0,1) wave mode for each thickness is nearly in the same phase for the plane pipe, whereas the phases of T(0,1) modes for the pipes with GRIN-PC lens are modified with the change in pipe thickness. The peak frequencies are 41.03 kHz, 42.82 kHz, and 43.07 kHz, respectively, for 6 mm, 4.75 mm, and 3.18 mm wall thicknesses. In the case with the GRIN-PC lens, the peak frequencies are 40.88 kHz, 41.82 kHz, 39.79 kHz, respectively, for 6 mm, 4.75 mm, and 3.18 mm. The signal obtained from the 6 mm-thick pipe has an initial leftward shift in the peak frequency to 41.03 kHz in the plain pipe case compared to the other two thicknesses, resulting in a different outcome than the numerical models. The numerical model was revised with the experimental pipe length of 1500 mm, indicating the reason for the shift in peak frequency as compared to the first numerical pipe length of 1067 mm. The trends of peak frequency versus pipe thickness are influenced by the difference in pipe lengths. Moreover, for the case of the pipe with the GRIN-PC lens, the peak frequency is affected by the pipe thickness due to composite behavior caused by stubs. Peak frequency is a useful feature that can be exploited to compare pipes of the same length, which would suit the purpose of uniform corrosion detection. However, since the length of the 6 mm pipe is different than the rest of the pipes, SDC is selected as the damage index as it is a quantity that is not affected by the length.

Based on the qualitative observation from Fig. 9(a) and 9(b), the experiments validate the change in dispersion characteristics for the T(0,1) mode dependent on the pipe thickness with the presence of the GRIN-PC lens. The phase difference in the T(0,1) window of the time domain signals were quantified by SDC. The baseline T(0,1) window obtained from the pipe with the 6 mm thickness was used as a reference to compute the SDC from different wall thicknesses using the following equation:

$$SDC = 1 - \left| \frac{cov(S_0, S_1)}{\sigma_0 \sigma_1} \right| \tag{5}$$

where $cov(S_0, S_1)$ represents the covariance between the baseline signal S_0 and the signal from each wall thickness S_1 , and σ_0 and σ_1 are the standard deviations of S_0 and S_1 , respectively. The overall relationship between the varying wall thickness and the SDCs for both the plain pipe and the pipe with the GRIN-PC lens is plotted in Fig. 10(a) and 10(b) for the numerical and the experiments results, respectively.

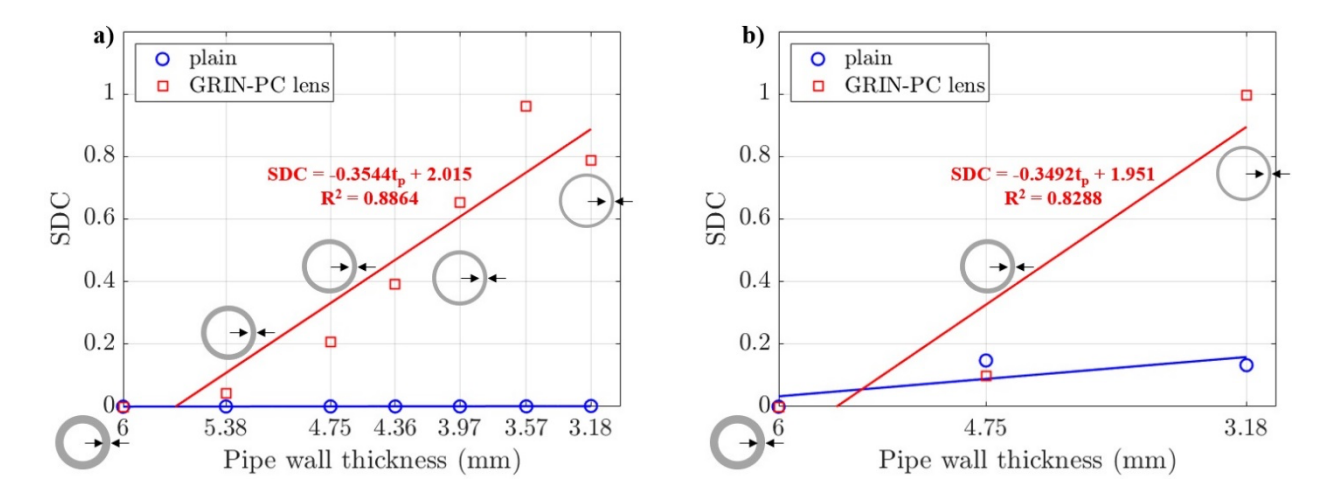


Fig. 10. Pipe wall thickness versus the SDC obtained from (a) the numerical models, and (b) the experiments.

The SDC values relative to the 6 mm pipe wall thickness were plotted with extra data points obtained from the full-scale numerical models with 5.38 mm, 4.36 mm, 3.97 mm, and 3.57 mm wall thicknesses, in addition to 4.75 mm and 3.18 mm. The SDC does not change for the case of the plain pipe, remaining perfectly at 0, whereas it gradually increases in the case of the pipe with the GRIN-PC lens. The relationship between pipe wall thickness and the SDC in the case with the GRIN-PC lens was quantified by linear polynomial fitting as indicated in Fig. 10(a). A

linear regression analysis was performed and the R² value was determined as 0.89. The SDC results from the experimental pipes are plotted in Fig. 10(b) along with the linear polynomial fitting. In the case of the plain pipe, the SDC values are 0.15 and 0.13 for the 4.75 mm and 3.18 mm thicknesses, respectively. There is an upward shift for these pipes relative to the original thickness, as a result of the different lengths of the 6 mm pipe, but their values remain approximately the same. In the case of the pipe with the GRIN-PC lens, the SDC values are 0.10 and 1.00 for the 4.75 mm and 3.18 mm thicknesses, respectively. The R² value is 0.83 in this case. The numerical data has a better fit with a higher R² value, compared to the experiments, due to the contribution of extra data points. Despite the underfitting of the experimental data, the slope and the y-intercepts of both linear models are approximately the same as the numerical data. The numerical and experimental results show that the change in SDC with the presence of the GRIN-PC lens is significant. Hence, the detection of overall thickness change simulating uniform corrosion becomes possible using the T(0,1) mode.

4. Conclusions

The phase velocity of the non-dispersive torsional wave mode T(0,1) in pipe-like structures is conventionally insensitive to thickness change. The integration of the GRIN-PC lens to pipe structure modifies the dispersion characteristics in favor of the T(0,1) wave mode, such that the detectability of thickness change can be achieved, according to the unit cell study. The unit cell results are supported by full-scale numerical models. For the same pipe lengths, the thickness variation can be tracked by using the peak frequency feature of the signal, as well as the damage index of signal difference coefficient relative to the original wall thickness. Experimental results with varying pipe length while keeping outer diameter the same show that there is a shift in the peak frequency depending on the pipe length. Therefore, the numerical models of finite pipe lengths with respect to wavelength need to consider actual pipe length with traction-free boundary conditions to match the experimental results. On the other hand, signal difference coefficient is less sensitive to pipe length while it becomes more sensitive to thickness variation if the pipe is designed with the GRIN-PC lens. The GRIN-PC lens is a mechanical lens without requiring any electronics. Hence, the GRIN-PC lens integrated with pipe provides an easy solution to make the T(0,1) mode more in favor by increasing the detectability of different defect

356 types. As future work, the influence of the GRIN-PC lens on the detection of localized defects in 357 pipe-like structures will be investigated with numerical models and experiments. 358 CRediT authorship contribution statement 359 Gorkem Okudan: Investigation, Data Curation, Visualization, Software, Writing – Original 360 Draft. Chenxi Xu: Validation, Writing – Original Draft. Hrishikesh Danawe: Methodology, 361 Writing – Review & Editing. Serife Tol: Conceptualization, Funding Acquisition, Supervision, 362 Writing – Review & Editing. **Didem Ozevin:** Conceptualization, Funding Acquisition, 363 Supervision, Writing – Review & Editing. 364 **Data statement** 365 The data can be provided upon request from the corresponding author. 366 **Declaration of Competing Interest** 367 The authors declare that they have no known competing financial interests or personal 368 relationships that could have appeared to influence the work reported in this paper. 369 Acknowledgment 370 This research was funded by the National Science Foundation under Award No. CMMI 371 1914663/1914583 entitled "Conformal Gradient-Index Lenses for Ultrasonic Wave 372 Amplification and Improved Diagnostics". The support from the sponsoring organization is 373 gratefully acknowledged. Any opinions, findings, and conclusions or recommendations 374 expressed in this material are those of the authors and do not necessarily reflect the views of the 375 National Science Foundation. 376 References 377 [1] C. I. Ossai, B. Boswell, I. J. Davies, Pipeline failures in corrosive environments – a 378 conceptual analysis of trends and effects, Eng. Fail. Anal. 53 (2015) 36–58. [2] S. Cunha, Comparison and analysis of pipeline failure statistics, in: 9th International Pipeline 379

380

Conference, 2012, pp. 521–530.

- 381 [3] S. N. Karlsdottir, Corrosion, Scaling and Material Selection in Geothermal Energy
- Production, in: A. Sayigh (Ed.), Comprehensive Renewable Energy, Elsevier, Oxford, 2012, pp.
- 383 241–259.
- 384 [4] G. H. Koch, M. P. H. Brongers, N. G. Thompson, Y. P. Virmani, J. H. Payer, Corrosion Cost
- and Preventive Strategies in the United States, NACE International: Houston, TX, USA, 2002.
- 386 [5] M. Askari, M. Aliofkhazraei, S. Afroukhteh, A comprehensive review on internal corrosion
- and cracking of oil and gas pipelines, J. Nat. Gas Sci. Eng. 71 (2019) 102971.
- 388 [6] M. Lowe, D. Alleyne, P. Cawley, Defect detection in pipes using guided waves, Ultrasonics
- 389 36 (1) (1998) 147–154.
- 390 [7] C. Jirarungsatian, A. Prateepasen, Pitting and uniform corrosion source recognition using
- acoustic emission parameters, Corros. Sci. 52 (1) (2010) 187–197.
- 392 [8] A. Joshi, L. Udpa, S. Udpa, A. Tamburrino, Adaptive wavelets for characterizing magnetic
- flux leakage signals from pipeline inspection, IEEE Trans. Magn. 42 (10) (2006) 3168–3170.
- 394 [9] K. Edalati, N. Rastkhah, A. Kermani, M. Seiedi, A. Movafeghi, The use of radiography for
- thickness measurement and corrosion monitoring in pipes, Int. J. Press. Vessels Pip. 83 (10)
- 396 (2006) 736–741.
- 397 [10] T. Jiang, L. Ren, Z.-G. Jia, D.-S. Li, H.-N. Li, Pipeline internal corrosion monitoring based
- on distributed strain measurement technique, Struct. Contr. Health Monit. 24 (11) (2017) e2016.
- 399 [11] J. L. Rose, J. Philtron, G. Liu, Y. Zhu, M. Han, A Hybrid Ultrasonic Guided Wave-Fiber
- 400 Optic System for Flaw Detection in Pipe, Appl. Sci. 8 (5) 727.
- 401 [12] F. Honarvar, F. Salehi, V. Safavi, A. Mokhtari, A. N. Sinclair, Ultrasonic monitoring of
- 402 erosion/corrosion thinning rates in industrial piping systems, Ultrasonics 53 (7) (2013) 1251–
- 403 1258.
- 404 [13] P. B. Nagy, F. Simonetti, G. Instanes, Corrosion and erosion monitoring in plates and pipes
- using constant group velocity lamb wave inspection, Ultrasonics 54 (7) (2014) 1832–1841.
- 406 [14] X. Zhao, R. L. Royer, S. E. Owens, J. L. Rose, Ultrasonic lamb wave tomography in
- structural health monitoring, Smart Mater. And Struct. 20 (10) (2011) 105002.
- 408 [15] K. R. Leonard, M. K. Hinders, Lamb wave tomography of pipe-like structures, Ultrasonics
- 409 43 (7) (2005) 574–583.
- 410 [16] E. Dehghan-Niri, S. Salamone, Quantitative corrosion imaging of pipelines using multi
- 411 helical guided ultrasonic waves, Struct. Monit. And Maint. 3 (2016) 215–232.

- 412 [17] J. L. Rodgers, W. A. Nicewander, Thirteen ways to look at the correlation coefficient, Am.
- 413 Stat. 42 (1) (1988) 59–66.
- 414 [18] X. Zhao, H. Gao, G. Zhang, B. Ayhan, F. Yan, C. Kwan, J. L. Rose, Active health
- 415 monitoring of an aircraft wing with embedded piezoelectric sensor/actuator network: I. Defect
- detection, localization and growth monitoring, Smart Mater. And Struct. 16 (4) (2007) 1208–
- 417 1217.
- 418 [19] H. Jiadong, J. Lin, L. Zeng, High-resolution damage detection based on local signal
- 419 difference coefficient model, Struct. Health Monit. 14 (1) (2015).
- 420 [20] W. Li, Y. Cho, Combination of nonlinear ultrasonics and guided wave tomography for
- imaging the micro-defects, Ultrasonics 65 (2016) 87–95.
- 422 [21] P. Deymier, Acoustic Metamaterials and Phononic Crystals, Springer-Verlag Berlin
- 423 Heidelberg, 2013.
- 424 [22] S. Q. Zhao, B. X. Liu, Y. Q. Wang, H. L. Chen, Vibration reduction of pipe systems using
- 425 phononic crystals, in: Manufacturing Process and Equipment, Vol. 694 of Advanced Materials
- 426 Research, Trans Tech Publications Ltd, 2013, pp. 354–360.
- 427 [23] D. Yu, J. Wen, H. Zhao, Y. Liu, X. Wen, Vibration reduction by using the idea of phononic
- 428 crystals in a pipe-conveying fluid, J. Sound and Vib. 318 (2008) 193–205.
- 429 [24] C. Gomez-Reino, M. V. Perez, C. Bao, Gradient-index Optics: Fundamentals and
- 430 Applications, Springer-Verlag Berlin Heidelberg, 2002.
- 431 [25] S.-C. S. Lin, T. J. Huang, J.-H. Sun, T.-T. Wu, Gradient-index phononic crystals, Phys. Rev.
- 432 B 79 (2009) 094302.
- 433 [26] H. Danawe, G. Okudan, D. Ozevin, S. Tol, Conformal gradient-index phononic crystal lens
- for ultrasonic wave focusing in pipe-like structures, Appl. Phys. Lett. 117 (2020) 021906.
- 435 [27] G. Okudan, H. Danawe, D. Ozevin, S. Tol, Torsional wave focusing in cylindrical structures
- with the conformal gradient-index phononic crystal lens, J. Appl. Phys. 129 (2021) 174902.
- 437 [28] C. Hakoda, J. L. Rose, and P. Shokouhi, Using Floquet periodicity to easily calculate
- dispersion curves and wave structures of homogeneous waveguides, AIP Conf. Proc. 1949
- 439 (2018) 020016 pp. 1–10.
- 440 [29] R. Carandente, Interaction between the Fundamental Torsional Guided Wave Mode and
- 441 Complex Defects in Pipes, Ph.D. Dissertation, Imperial College, 2011.

- 442 [30] H. Yalcinkaya, D. Ozevin, The Design and Calibration of Particular Geometry Piezoelectric
- 443 Acoustic Emission Transducer for Leak Detection and Localization, Meas. Sci. Technol. 24
- 444 (2013) 095103.